Testing Os staining approach for visualizing soil organic matter patterns in intact samples via X-ray dual-energy tomography scanning

Hongbing Zheng[12], Kyungmin Kim[1], Alexandra Kravchenko[1]*, Mark Rivers[3], Andrey Guber[1]

[1] Department of Plant, Soil and Microbial Sciences, Michigan State University, East Lansing, MI, United States,

[2] Research Institute of Agricultural Resources and Environment, Jilin Academy of Agricultural Science, Changchun, 130033, China;

[3] Argonne National Lab, Center for Advanced Radiation Sources, the University of Chicago, Chicago, IL, United States

***Corresponding Author:**

Department of Plant, Soil and Microbial Sciences, Michigan State University, East Lansing, MI, 48824, United States.

E-mail: kravche1@msu.edu

Abstract

Challenges with *in situ* visualization of non-particulate organics in porous materials limit understanding and modeling processes of transport, decomposition, and storage of organic compounds. In particular, it impedes deciphering the mechanisms driving accumulation and protection of soil organic matter (SOM), processes crucial for sustaining soil fertility and mitigating effects of global climate change. A recently proposed method of staining soil organics by OsO_4 vapors with subsequent dual-energy X-ray computed micro-tomography scanning (μCT) offers new opportunities to visualize SOM within intact soil matrix. Our objective was to test the method's performance in staining different organic materials located in media with contrasting

pore characteristics: 1) roots of switchgrass (*Panicum virgatum* L.), either placed within fine and coarse sands or grown within soil micro-cores, 2) biochar fragments, and 3) soils with relatively low and high C contents. We found that the method was effective in staining organic materials of root origin and the organics associated with fine soil particles, but not the biochar. The estimated percent of total C that reacted with OsO_4 vapors ranged from 0.7% in plant roots to 3.2% in sand-free fraction of the high C soil and was only 0.2% in the studied biochar. Total soil C and Os concentrations were strongly linearly related, suggesting a potential for future method development. However, we would recommend caution when interpreting the results in cases when gas diffusion through the soil matrix is limited.

Key words: Soil organic matter, Os staining, dual-energy X-ray computed micro-tomography, roots, biochar

INTRODUCTION

Soil organic matter (SOM) is the main contributor to soil quality and productivity, as well as the most important indicator of soil sustainability [1-4]. Various soil functions, including tilth [5], fertility [6], and hydrology [7] are associated with SOM. Understanding the mechanisms driving SOM protection and accrual is vital for effective soil management and soil carbon sequestration.

Physical barriers between SOM and its microbial decomposers is one of the mechanisms of SOM protection [8, 9]. While studies of soil aggregates convincingly demonstrated the importance of physical protection [10], its assessment and quantification in intact soil matrix remain challenging [11], due, in part, to difficulties in measuring SOM in a spatially explicit context. Lack

of quantitative data on SOM locations within intact soil limits opportunities for studying the mechanisms of its protection and accrual and impedes process-based modeling and predictions.

X-ray computed micro-tomography (μCT) allows visualization of large organic fragments, such as particulate organic matter (POM) and plant roots in intact soil samples[12-15]. However, visualization of non-particulate SOM is problematic and, until recently, possible only in very small, e.g., sub-millimeter, intact soil samples (e.g., [16, 17]).

Peth et al. (2014)[18] proposed a new method of *in situ* SOM visualization, which can be implemented on intact soil samples up to a few centimeters in size. The method is based on the ability of osmium tetroxide, OsO_4, to react with organic substances, in particular, lipids. Specifically, an air-dry soil is subjected to OsO_4 vapors, which, upon diffusion into the soil, bind with organic materials, staining them [19]. The presence of Os within the stained soil is then determined from dual energy X-ray μCT. The sample is scanned at two energies − above and below the *K*-edge energy of Os − and the locations of the organic materials to which Os bonded can be identified from the differences between the above- and below-*K*-edge images. Rawlins et al. (2016)[20] were the first to use the new approach to explore patterns of SOM distributions as a function of soil pores. While the method shows substantial promise in revolutionizing SOM visualization in intact soil samples[18, 20, 21], an assessment of its utility under diverse range of soil conditions has been lacking, deterring wide utilization of this innovative technique. Here we explored the capabilities of SOM visualization via Os-staining and proposed a method of quantitative conversion of image results into volumes of reacted Os. The conversion enables assessments of the proportions of organic materials present in the soil that can be visualized by the procedure.

The Os-staining approach has two limitations, which can potentially reduce its effectiveness for quantitative assessment of SOM levels. The first limitation: while it has been long known that it is unsaturated or double bond C primarily involved in Os-staining process, the details on prevailing chemical reactions are still as elusive as 50 years ago [22] and remain a subject of active research [23]. A variety of unsaturated compounds, including amino acids and proteins, can be stained [24] and SOM is a heterogeneous complex mixture of organic molecules of microbial, plant, and animal origin [25] with only a portion of them represented by unsaturated C. The second limitation: the effectiveness of the staining depends on the diffusion of OsO_4 vapors within the soil. The organic compounds located in the areas within the soil matrix inaccessible to gas diffusion will not be stained.

The goal of this study is to examine the effect of these limitations on performance of Os staining approach for SOM visualization. The study addresses two main research questions. First, how effective is the Os method in staining three organic sources typically present within the soil matrix: plant roots, biochar, and SOM associated with fine soil particles. We hypothesized that a lack of unsaturated C bonds in biochar will result in low effectiveness of its Os-based visualization. Second, how pore-size distribution influences Os staining of SOM. We hypothesized that lower porosity will impede Os vapor diffusion and thus result in less effective staining.

MATERIALS AND METHODS

Experiment 1. Os-staining of Organic Matter Inclusions. The experiment consisted of staining by Os three types of organic materials, commonly present in agricultural soils, placed within two sand media with contrasting pore-size distributions. The three studied materials were 1) air-dried

93 roots of switchgrass (*Panicum virgatum* L.), 2) biochar fragments, and 3) inclusions of high C soil
94 (Houghton series, Typic Haplosaprists). The root fragments were taken from air-dried root mass
95 of field collected switchgrass plants; the root fragments used in this study were approximately 1
96 mm in diameter and 3 mm in length, with the average weight of a root fragment of 0.10 mg. The
97 biochar was made from switchgrass; the biochar fragments used in the study were ~2x2x2 mm in
98 size, with the average fragment weight of 0.08 mg. The high C soil for the study was collected
99 from 0-5 cm depth in a formerly drained wetland turned into an agricultural field in Central
100 Michigan, USA. Soil texture was silt loam with 28% sand, 57% silt, and 15% clay. The total
101 porosity was equal to 58%. The average weight of soil used as a single inclusion was 1.6 mg. Total
102 C and N levels of the three studied organic materials are presented in Table 1.
103

104 **Table 1.** Total C and N data of the three organic materials used for assessing Os staining efficiency
105 in Experiment 1 and soil used in Experiment 3. Shown are means and standard deviations in
106 parenthesis (n=5).
107

Organic material	C, %	N, %	C/N
Switchgrass roots	39.4 (0.5)	1.00 (0.05)	39.5 (2.4)
Biochar	64.9 (3.7)	0.65 (0.33)	125 (60)
High C soil	3.14 (0.17)	0.54 (0.03)	5.8 (0.5)
Low C soil	1.17 (0.012)	0.12 (0.001)	9.7 (0.09)

108

109 The two studied sand media had particle sizes of 2-3 mm and 53-100 μm (hereafter called
110 "coarse" and "fine" sands, respectively). The coarse sand was Ottawa Standard sand (20-30 mesh)
111 acquired from Spectrum Chemical Corp. In order to ensure that the two media were of the same
112 mineralogical composition, the fine sand was derived from the coarse sand by grinding. The pore
113 characteristics of the two media were obtained from X-ray μCT images as described further. The

114 image-based porosities (i.e., volumes of pores > 5.7 μm) of the coarse and fine sands were equal
115 to 37% and 19% of the total volume, respectively. Their image-based pore-size distributions were
116 dominated by pores with radii in 30-170 μm and 6-12 μm range, respectively (Fig.1). The total
117 porosity calculated from the bulk density of the coarse and fine sands and assuming particle density
118 of 2.65 g cm^{-3} was equal to 56% and 57%, respectively. Therefore, the pores < 5.7 μm occupied
119 19% and 28% of the total volume in the respective sands.
120 The samples were assembled within hollow plastic spheres of 7.5 mm Ø opened from one
121 end (Fig. 1). The organic materials were placed as individual inclusions within the sand medium.
122 Each sphere contained three organic inclusions of the same type located at distances of 2, 4, and 6
123 mm from the opened end. This set-up enabled assessing Os staining of the inclusions at three
124 different lengths of diffusion paths. A total of 12 spheres, 2 replications for each combination of
125 the organic material and sand type, were prepared. During sphere preparation, first, a ~1 mm layer
126 of sand was placed on the bottom, the first organic fragment was inserted in the center of the sand
127 and covered with another layer of sand 2 mm deep. Then, the second organic fragment was placed
128 in the sand, followed by the third sand layer and the third piece. The third piece was covered with
129 the remaining sand up to the top of the sphere. After assembling, the spheres were subjected to
130 staining by OsO_4 vapors, as described further.
131 After the staining, the tops of the spheres were covered with lids that were glued-on to
132 ensure that the arrangement of sand and organic inclusions within the spheres was not disturbed.
133 Each sphere had a shaft that was used to keep it in a vertical position during X-ray μCT scanning
134 (Fig. 1c). Such experimental set up enabled us to maximize the information that could be obtained
135 from a narrow X-ray μCT scanning window available at that time at Argonne National Laboratory
136 for Os energies, as described further. The area within the sample where Os could be reliably

identified was only ~2 mm high because of limitations on the synchrotron beam height. Thus, the spheres were built and saturated with OsO_4 vapors in a horizontal position, which created a range of distances between the surface, i.e., the point of gas entry, and the organic inclusions. During scanning the spheres were placed in a vertical position so that the three organic inclusions were all located within the 2 mm high central portion of each sphere, thus within the region of reliable Os identification.

Experiment 2. Os-staining of sand/soil mixtures. The purpose of the experiment was to assess the overall spatial patterns of Os distribution generated due to gradients in OsO_4 diffusion within the scanned spheres. The experiment consisted of three spheres, each filled with a material with different organic C level, thus representing an organic C gradient: the high C soil (the same soil as that used for inclusions in Experiment 1), the high C soil 50:50 mixed with the fine sand (the fine sand used in Experiment 1), and the fine sand only. The soil was homogenized by gentle grinding so that no large aggregates remained. The spheres were subjected to Os staining, then the lids were glued on, and the X-ray μCT scanning was conducted.

Figure 1. Illustration of the set-up for Experiment 1. **A**. Examples of spheres filled with fine and coarse sands. To ensure stability during sand filling the spheres were held within foam-rubber cubes (on the right). **B**. Schematic representation of the locations of the organic inclusions within the sphere. Note that the view is through the center of the sphere. **C**. The sphere with the lid glued-on, ready for X-ray µCT scanning. **D.** Pore size distributions for the image-based (>5.7 µm) pores in fine and coarse sand materials used in Experiments 1 and 2. Pore size distributions were obtained using Beat plug-in of ImageJ.

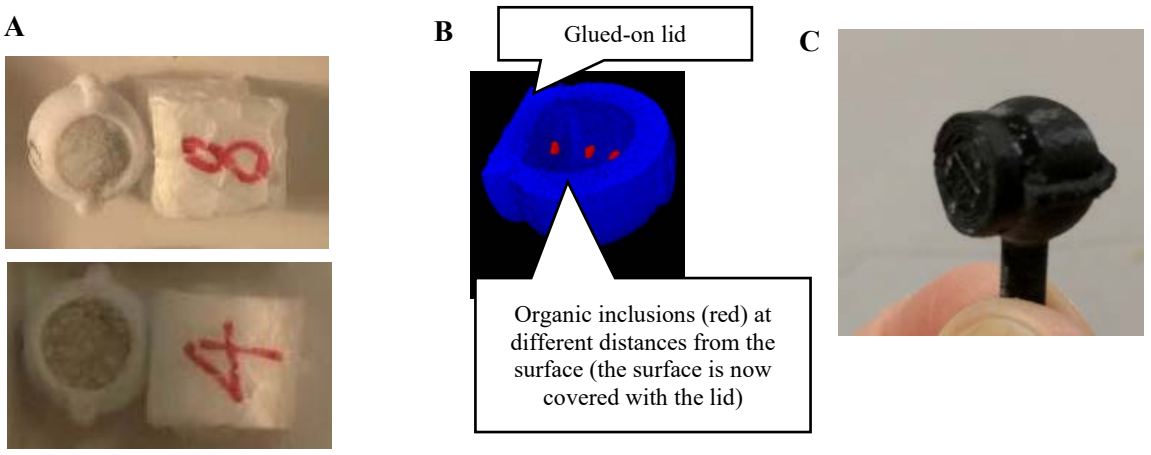

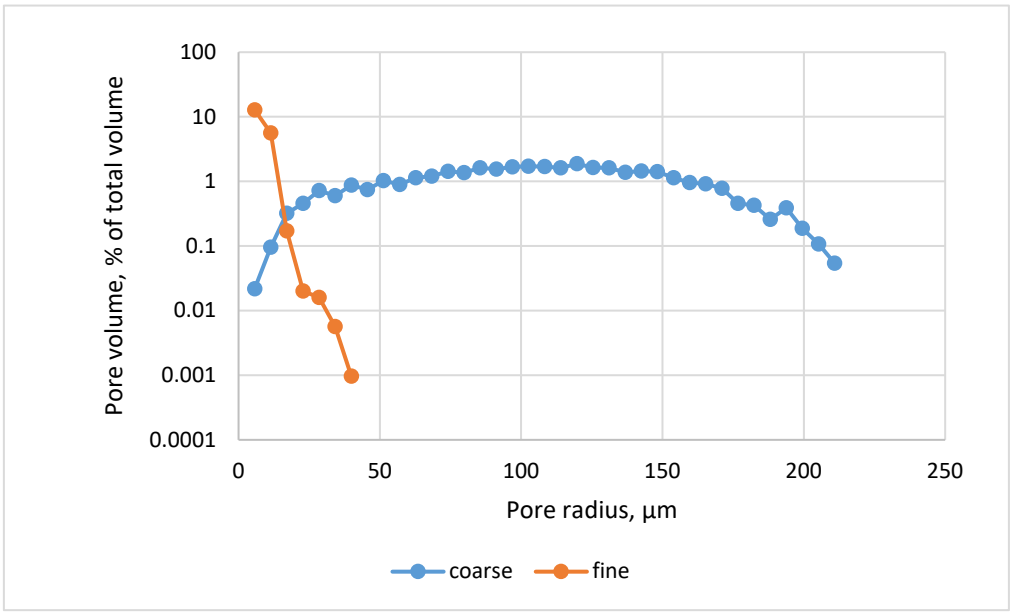

Experiment 3. In-grown plant roots in soils with contrasting pore characteristics. The purpose of the experiment was to explore Os staining of plant roots naturally grown within the soil matrix. The experiment studied two soil materials with contrasting pore characteristics. The soil for the experiment was collected from conventionally plowed experimental agricultural field of Long Term Ecological Research site at the Kellogg Biological Station, Michigan, USA, from 5-15 cm depth. The dominant soil series at the site are Kalamazoo and Oshtemo (mesic Typic Hapludalfs)[26]. Soil was air-dried for a week and then sieved to procure 1-2 mm aggregate fraction. Half of the collected 1-2 mm fraction was gently ground, first by mortar and pestle and then with a shatter box, to generate material with < 0.5 mm particle sizes. The 1-2 mm original fraction was a sandy loam with 58% sand, 35% silt and 7% clay, while the generated smaller fraction was a silty loam with 35% sand, 56% silt and 9% clay. These fractions constituted the two soil materials with contrasting pore size distributions but with the same mineralogy and other soil characteristics. Previous testing of the soil materials procured using this approach conducted by our research team demonstrated that the pore size distribution of the 1-2 mm material was dominated by >30 μm pores, while that of the <0.5 mm material was dominated by < 10 μm pores [27]. The two materials are hereafter referred to as large pore and small pore soils, respectively.

A 2.35 g of the generated soil materials was packed in 8 mm Ø, 3.75 cm length cylindrical tubes to the density of 1.25 $g \cdot cm^{-3}$. A total of 16 soil tubes were used: 9 for large and 7 for small pore soils. Switchgrass (var. Cave-In-Rock) plants were grown in the tubes, one plant per tube, for 4-5 weeks. To facilitate germination, prior to planting, the switchgrass seeds were shaken for 5 minutes in 8 M H_2SO_4. Seeds were then rinsed with distilled water 3 times and placed into a petri dish, with Whatman #1 filter paper (Sigma-Aldrich, U.S.A) soaked with 5 mL sterile 0.2 % KNO_3 inside. Seeds were distributed evenly on the petri dish, and another filter paper was placed onto

191 them. Petri dish was sealed with parafilm, covered with aluminum foil, and placed into 4 ºC
192 refrigerator. After 3-7 days, the germinated seeds were placed on the soil packed in the tube, one
193 seed per tube. During plant growth the moisture level within the tubes was kept at approximately
194 60% water-filled pore space. The plants were terminated by cutting the shoots and air-dried prior
195 to Os staining.
196
197 **Os staining.** For staining the samples from all three experiments were placed in a 78.5 mL glass
198 container with a 50 mm Ø watch glass in the center. Four mL of 2% OsO_4 solution was pipetted
199 into the watch glass and the container was sealed. The samples was exposed to OsO_4 vapors,
200 entering them from the surface, for a period of one week, during which the OsO_4 solution was
201 replenished to its original level every two days, with a total of ~12 ml of OsO_4 solution used per
202 container. The amount of OsO_4 vapors generated during this period was significantly in excess of
203 the amount required to react with all organic matter estimated to be present with the samples[28].
204 The exposure time was also significantly in excess of the time needed for OsO_4 to diffuse and fill
205 the whole pore space within the studied samples[18]. Because OsO_4 is highly poisonous, the staining
206 and all OsO_4 manipulations were conducted under the fume hood.
207
208 **X-ray µCT scanning.** The image data were collected on the bending magnet beam line, station
209 13-BM-D of the GeoSoilEnviroCARS at the Advanced Photon Source, Argonne National
210 Laboratory. All samples were scanned at two energies: 74.0 and 73.7 keV, above and below the
211 Os *K*-edge, respectively; at 5.7 µm resolution. Each reconstructed three-dimensional image
212 consisted of 240 slices with 1,920 by 1,920 pixels per slice. The limitation to 240 slices (1.37 mm)
213 arose from a limitation of the beamline monochromator, which was operating near its maximum

energy, and more than 60% of the beam was spilling off the second crystal. The monochromator has subsequently been improved so that the beam at this energy is now 3.0 mm tall.

µCT image analysis. The image analyses were conducted using ImageJ/Fiji[29, 30]. Differences between above and below *K*-edge images were calculated for every sample using the Image Calculator tool. Osmium concentrations were calculated in voxels of the resultant images as:

$$S_{Os} = \Delta G/(F \cdot r \cdot \Delta\mu) = 0.226 \cdot 10^{-3} \cdot \Delta G \qquad (1)$$

where S_{Os} is the Os concentration in image voxels ($g \cdot cm^{-3}$); ΔG is the difference in grayscale values (GV) between the above- and below *K*-edge images [-]; *r* is the voxel length in the sample calculated as the pixel size of the Grasshopper camera divided by the magnification of the lens used to image the scintillator (5.7 µm); *F* is the conversion coefficient for GVs from floating point to 16-bit integer values on images (10^6); $\Delta\mu$ is the difference between the photon mass attenuation coefficients μ/ρ [31] corresponding to the above and below *K*-edge energies for Os (7.75 $cm^2 \cdot g^{-1}$).

Image analyses for Experiment 1: First, we created the masks of the organic inclusions based on the below *K*-edge images. For that the images were subjected to filtering via Denoising, followed by Gaussian Blur 3D filter with 2x2x2 window, and the Enhance contrast tool with 0.6% saturated pixels setting. Then the range of GVs that corresponded to the lower and upper boundaries of the material within the inclusions were identified manually and used as lower and upper boundaries for thresholding. Besides identifying the inclusions, the thresholding also produced partial volume effect artifacts, primarily on boundaries of sand and air. To remove them we identified the boundaries using Find Edges tool applied to the respective below *K*-edge images, and then thresholded and removed the edges. Several 3D Erode steps were applied to

remove any remaining large artifacts, followed by Particle Analyzer of BoneJ to separate the inclusions from any lingering artifacts. Note that the sand grains within the soil inclusions were excluded during the thresholding, thus the data for the high C soil inclusions from this experiment represent the sand-free soil. The inclusions were converted into binary masks. The masks were applied to the above-below *K*-edge difference images by multiplying one by the other in the Image Calculator tool. No denoising or filtering were applied to the difference images. The grayscale values (ΔG) from the difference images corresponding to the mask of each organic inclusion were used in further analyses.

In addition to the organic inclusions within each image, we also selected an area (4.4 x 1.3 x 1.2 mm^3) that consisted only of the sand material. Both for the organic inclusion masks and for the sand-only area we calculated the average ΔG values from the difference images and then converted them in Os concentrations, S_{Os}, using Eq. (1).

Image analyses for Experiment 2: The average S_{Os} levels were calculated in the central portions (12 mm^3) of the spheres' above-below *K*-edge difference images using Eq. (1). No denoising or filtering were applied to the difference images. The top 1 mm portions of the above-below difference images were excluded from further analyses, since the sample top could not be packed to the same level of density as the rest of the sample, affecting the spatial pattern of GVs.

The overall patterns of S_{Os} distribution within the spheres were obtained from the difference images using Remove Background tool of Xlib/Beat[32, 33]. The tool extracts the background signal and enables retrieving the difference signal as a function of distance. The second order polynomial regression equations were fitted to the difference images using the Remove Background tool. The obtained regression equations reflected the general spatial trends in S_{Os} distributions as a function

of the distance from the surface of the sample. The central 4.8 x 4.8 mm portion of each sphere was used in the overall pattern analysis with the vertical depth of 1 mm.

Image analyses for Experiment 3: Due to high level of noise in the images from Experiment 3, prior to the analyses, the above-below difference images were subjected to noise-reducing Median 3D (radius = 2) and Gaussian blur 3D (4x4x4 window) filters.

To calculate S_{Os} in the soil matrix and in the switchgrass roots, binary mask images of soil matrix and roots were obtained from the below *K*-edge images. For creating soil matrix binary masks we used ImageJ's built-in 'default' thresholding method; for creating root binary masks we used the minimum error thresholding method[34]. Partial volume effects were removed as described above. S_{Os} values separately in the soil matrix part of the sample and in the roots were obtained by multiplying the above-below *K*-edge difference images by the respective binary masks using Image Calculator tool of ImageJ and applying Eq. (1).

Quantification of C that responded to OsO_4 presence. The Os staining is primarily based on the reaction between OsO_4 and olefinic double bonds. The reaction leads to formation of Os mono- and di-esters, which, in case of unsaturated lipids and phospholipids, involves Os binding to single or double chains of unsaturated fatty acids [35]. The Os staining reactions can also involve formation of oxo bridges and connecting electron donor groups from amino acids (from Belazi et al., 2009[23] (based on [36, 37])).

The number of Os atoms, N_{Os}, that remained within 1 cm^3 of the scanned sample, after the staining and binding to the organic molecules, at the time of μCT scanning, can be estimated as:

$$N_{Os}=S_{Os}/(190.23/N_A), \quad \text{Eq. (2)}$$

where S_{Os} is the Os concentration as determined by Eq. (1), 190.23 is the atomic weight of Os [g mol^{-1}], and N_A is the Avogadro constant ($6.02x10^{23}$ mol^{-1}). Assuming that each OsO_4 molecule reacted with either two or four C atoms (from Belazi et al., 2009[23] (based on [36, 37])), the number of C atoms that were involved in interactions with OsO_4 can be estimated as ranging from $2N_{Os}$ to $4N_{Os}$, with its C concentration [g cm^{-3}] ranging from $2N_{Os}$ x 12/ N_A to $4N_{Os}$ x 12/ N_A. Knowing the total C content of the specific organic material, we can assess the percent of C in it that was involved in reactions with OsO_4 during staining. The calculations for the studied materials are reported in Appendix Table 1. For these calculations we obtained the density of coarse and fine sands and soils by measuring the weight of these materials packed within a given volume. Density of roots and biochar used in the inclusions were calculated from the weight of the individual inclusions and their volume as determined from the μCT images. Note that only few inclusions were completely within the 2 mm field of scanning view, thus the density estimates are based on averages of 2-3 individual inclusion pieces.

Statistical analysis. The statistical model for the S_{Os} data from Experiment 1 consisted of the fixed effects of the sand type, organic material type in the inclusions, position within the sphere, and their interactions. The random effect of the sphere nested within the sand and organic material types was used as an error term for testing the main effects of these two factors. The Experiment 2 samples were intended for the overall visualization of Os patterns; thus, no formal statistical analyses were performed for them. The statistical model for Experiment 3 data analysis consisted of the fixed effects of soil pore size (large and small), the medium (soil matrix and roots), and their interaction. The random effects of soil tubes nested within the pore size were used as an error term to test the effect of the pore size. Data analyses were conducted using the

mixed model approach implemented in the PROC MIXED procedure of SAS Version 9.4 (SAS Inc, 2009).

RESULTS

Examples of the scanned images from Experiment 1 are shown on Fig. 2. We present side-by-side the images obtained at below Os *K*-edge energy and the above-below *K*-edge difference images. The images below Os *K*-edge energy illustrate the observed patterns in the sand with the organic inclusions encountered in Experiment 1 (Fig. 2). Brighter colors on the difference images represent higher GVs, corresponding to greater Os levels. The root fragments were clearly visible in the difference images (Fig. 2 right), both in the coarse and fine sands. The organic soil inclusions also had distinctly brighter colors than the background in the difference images (Fig. 2 right). Note the sand grains belonging to the soil inclusions - bright and highly visible on the below Os *K*-edge images due to their high density, but dark on the difference images due to complete absence of Os within them. Unlike roots and soil inclusions, the biochar fragments were only weakly discernible over the background noise.

Figure 2. Selected sample images from the spheres in Experiment 1 with the organic inclusions in coarse and fine sands. On the left are the images at 73.7 keV energy (below Os *K*-edge) and on the right are the images of the above-below *K*-edge differences. Within each difference image the brighter grayscale values correspond to higher Os presence. Red arrows mark position of a large sand grain from soil inclusions on both images.

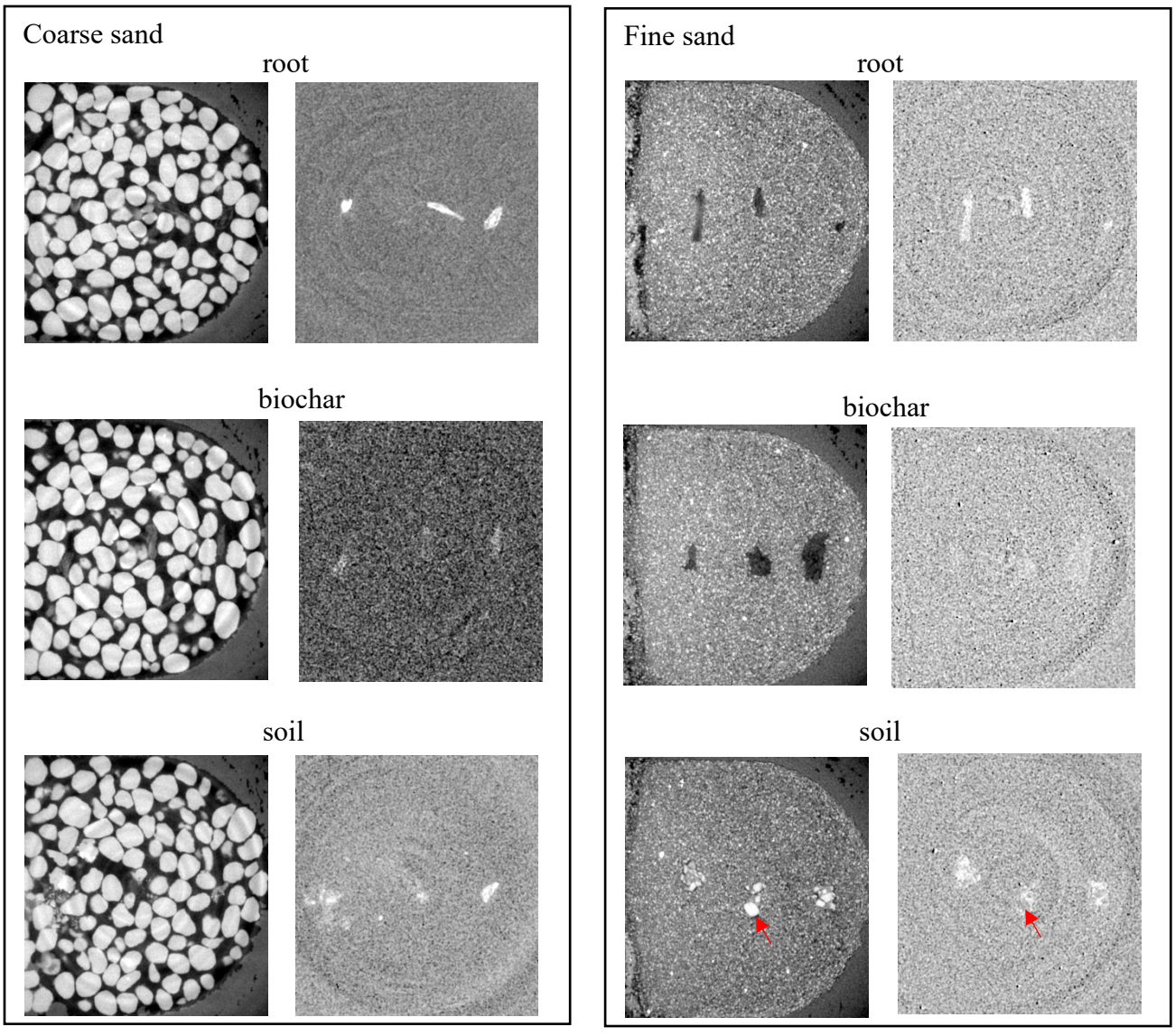

Figure 3. Sample images from the study's experiments. A) The sphere filled with high C soil from Experiment 2. On the left is the image at 73.7 keV energy (below Os *K*-edge) and on the right is the image of the above-below *K*-edge difference. Red arrows mark the position of a large stone on both images. Yellow arrows mark the position of a POM fragment on both images. B) In-grown switchgrass roots in a large-pore soil tube (top) and a small-pore soil tube (bottom) from Experiment 3 and their respective above-below *K*-edge difference images on the right. Soil matrix parts are brown, while roots are marked green for better visualization. Yellow arrows mark the points on the difference images that correspond to the roots.

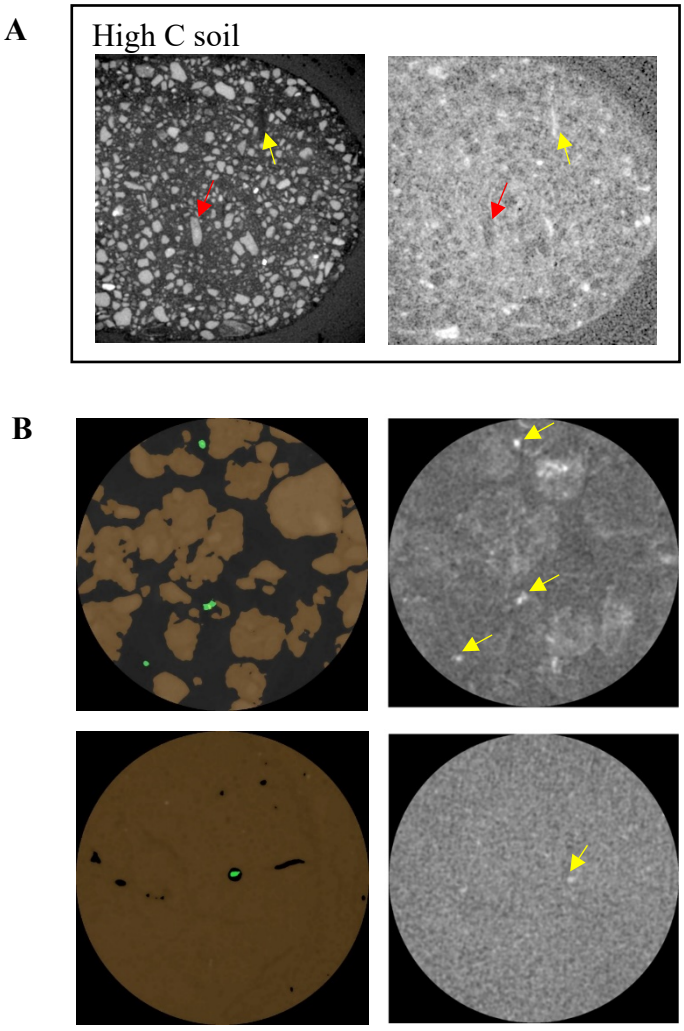

Numerous fragments of POM and possibly plant root remains were also clearly distinguished by their bright color on the difference image of the soil from Experiment 2 (Fig. 3A), reflecting their high S_{Os} levels. The large mineral particles (sand and small stones) were distinctly dark due to absence of Os. The remaining soil matrix had an intermediate range of GV levels varying substantially within the sphere and likely reflecting variations in the levels of the SOM connected to fine soil particles with unsaturated C bonds (Fig. 3A).

Analysis of Os-staining of organic matter inclusions in Experiment 1 showed that the Os concentrations within the soil inclusions were significantly higher than those in the biochar fragments both in the coarse and fine sands ($p<0.05$) (Fig. 4). In the coarse sand the Os in the roots greatly exceeded that in the soil and the biochar inclusions ($p<0.05$), while in the fine sand the Os in the roots were numerically in-between the biochar and soil values, while not statistically significantly different from each other. The Os levels in the roots were markedly greater in the coarse than in the fine sand. Coarse sand's Os levels were numerically higher than those in the fine sand for the 2 mm and 6 mm distances from the surface in the biochar and soil inclusions (statistically significant for soil at 6 mm distance). But there were no differences between the two sands for 4 mm distance in both soil and biochar. The distances between the organic inclusion and the surface did not influence Os concentrations for either of the three studied materials.

Figure 4. Os levels, S_{Os}, as calculated from Eq. (1), within the biochar, root, and soil inclusions in the two studied sand materials at the three studied distances from the surface. Shown are means and standard errors (n=2). Stars mark the statistically significant differences between the two sands within each distance of each material ($p<0.05$), not-significant differences between the two sands are unmarked. Different letters mark the materials that are statistically significantly different from each other within the same distance of the same sand type ($p<0.05$).

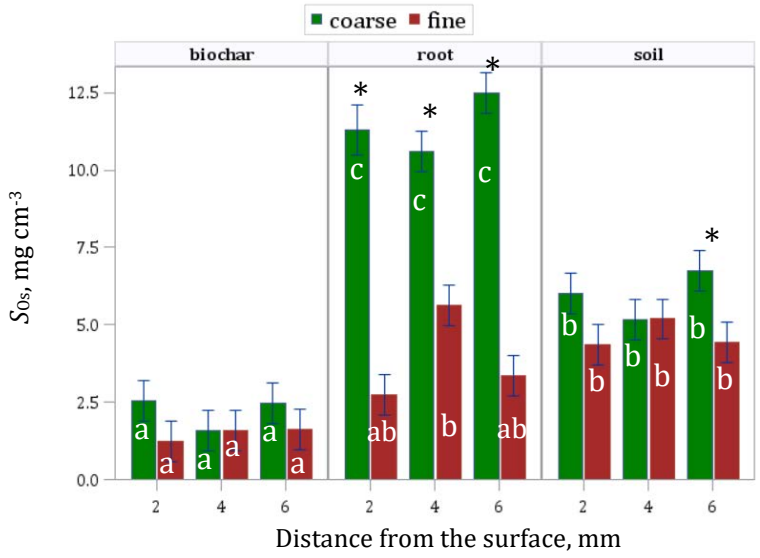

Experiment 2 showed that the average Os concentration in the soil-only sphere, 3.8 mg cm^{-3}, was approximately twice that of the 50:50 sand-soil mixture, 2.0 mg cm^{-3}, while the levels in the fine sand-only sphere fluctuated around zero (Table 2 and Fig. 5). The Os concentration distribution as a function of surface distance followed a quadratic trend (Fig. 5). Lower Os at 2-3 mm from the surface probably reflected lower density in the top parts of the spheres and some shifting of the material there during transport. The decrease towards 5-6 mm depths in the soil-only and, to a lower extent, in the sand-plus-soil mixture probably reflected the limitations to Os diffusion.

Figure 5. Quadratic regression trends of the Os concentrations, averaged across the central portions of the spheres (4.8 x 4.8 x 1 mm), plotted versus the distance from the surface of the sample exposed to OsO_4 vapors. Circles represent the average grayscale image values for each distance.

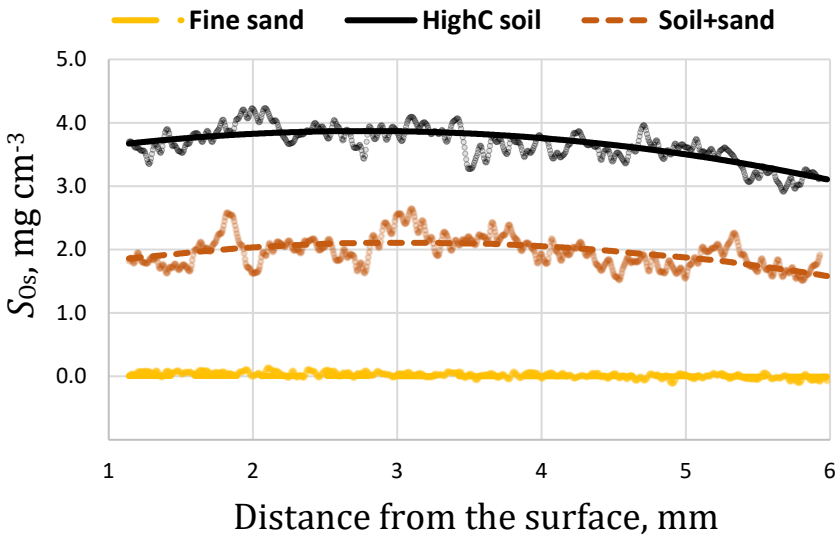

Results of Experiment 3 demonstrated that the Os concentration in the roots (~10 mg·cm^{-3}) was significantly higher as compared to the concentration in the soil matrix (~1.1 mg·cm^{-3}). The pore size distribution did not influence the Os concentrations in the soil matrix nor roots (Fig. 6).

According to our assessment, the C that reacted with OsO_4 during the staining experiments of this study constituted 0.7% of the total C in the switchgrass roots, and approximately 3% and 2% of the total C in the high C and low C soils, respectively. It only constituted 0.2% of the C within the studied biochar (Table 2).

Figure 6. Os levels, S_{Os}, as calculated from Eq. (1), in the soil matrix and in-grown switchgrass roots within the tubes with soil materials dominated by large- and small-pores. Symbol * marks the significant difference between the soil matrix and the roots in the given pore sizes ($p < 0.05$, n=7~9). The differences between large- and small-pore materials were not statistically significant either for soil matrix or roots.

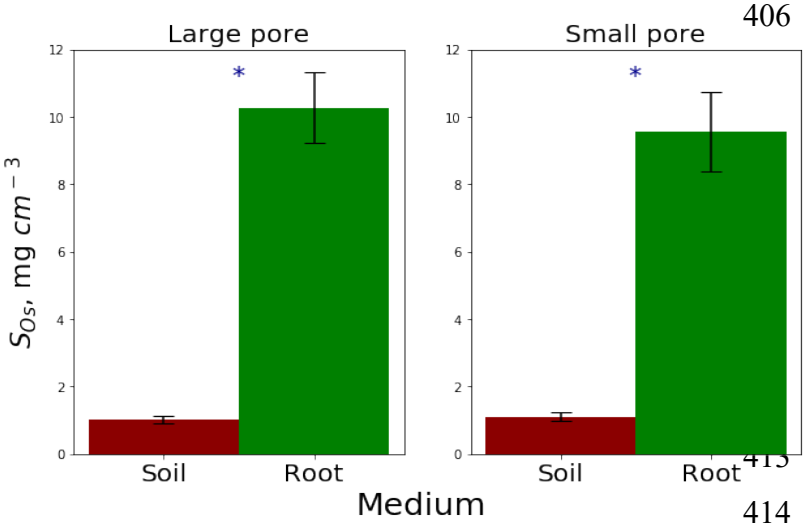

Table 2. Os concentrations, S_{Os}, as calculated from Eq. (1), and estimated % of total C involved in reactions with Os in the studied materials. Shown for S_{Os} are means and standard errors for data from Experiment 1 and 3 and individual values from Experiment 2. NS marks the means that were not significantly different from zero (p<0.05). Mean S_{Os} levels were used for % of total C estimates.

Material	**Os, mg cm^{-3}**	**% of C that responded to Os**
Switchgrass roots	8.4 (1.2)	0.7
High C soil, sand free	5.3 (1.2)	3.2
High C soil, bulk	3.8	2.9
High C soil + fine sand (50:50)	2.0	3.0
Low C soil	1.2	2.2
Biochar	1.8 (1.2) NS	0.2
Fine sand	-0.04 (1.0) NS	
Coarse sand	-0.19 (1.1) NS	

DISCUSSION

The Os-staining method stained both the organic materials of root origin, that is root-originated particulate organic matter, and the organics associated with fine soil particles, that is, non-particulate soil organic matter. It was less successful in visualizing biochar, even though most of the biochar fragments were still somewhat, even though not highly, Os stained.

These findings recommend Os staining as a promising method for 3D SOM visualization in cm-sized intact soil samples[18, 20, 21]. While several approaches have been proposed for 3D visualization of POM with X-ray μCT, using either distinct GVs of organic materials [38] or staining large organics with different staining agents[15], so far, visualization of non-particulate soil C has been achieved only in very small samples, i.e., tens- to hundreds-of-microns, with STXM-NEXAFS[1] (e.g., [39, 40]) or NanoSIMs[2] (e.g., [17]), and that in 2D only. The 3D visualization of SOM in intact samples of relatively large sizes, e.g., one- to few centimeters, has not been possible. Os staining with dual-energy X-ray μCT offers new research opportunities for exploring C processes and generating new insights regarding soil C protection and accumulation[18, 20] in intact soil samples of the sizes that are regarded as representative of the entire soil matrix[41, 42].

However, our findings also call for caution in interpretation of Os-staining results. The method's performance depends on the composition of the materials constituting the studied organics. Our results demonstrate that only a small fraction of the root fragments and of the SOM responded to Os presence (Table 2). Root tissue is dominated by cellulose, which does not have double C bonds reacting with Os, while lipids and amino acids, despite their functional importance, constitute only a minor proportion of the total root C. SOM is a complex mixture of biopolymers

[1] scanning transmission x-ray microscopy coupled with near edge x-ray absorption fine structure spectroscopy

[2] high-resolution secondary ion mass spectrometry

443 of plant and microbial origin and their degradation products, including proteins, carbohydrates,
444 aliphatic compounds, and lignin [43-46]. Present in the plant-derived compounds are aromatic,
445 phenolic and carboxylic C groups (Dhillon et al., 2017), while aliphatic-C and C=N bonds of
446 imidazol structures, carboxyl/carbonyl-C, amide- and O-alkyl-C functionalities dominate in
447 organic C isolated from soil fungal and bacteria [47, 48]. All these compounds and C groups do not
448 readily react with OsO_4. Thus, it is not surprising that such small portion of the present C could
449 be directly identified via Os staining (Table 2). Our observations agree with 0.02 Os:C atomic ratio
450 reported for Os stained cell tissues in a course of scanning transmission electron microscopy[49].
451 Very low Os staining of biochar (Fig. 4, Table 2) supported our initial hypothesis. Biomass
452 pyrolysis during biochar production leads to depletion of double C bonds and prevalent formation
453 of aromatic polycyclic structures dominated by benzene rings [50].

454 Nevertheless, our observations suggest that it might be worth the effort to explore
455 possibilities for the Os method as an empirical tool for quantifying organic C distribution patterns
456 within intact soil samples. In this study we examined 4 soil materials representing a gradient of
457 levels of non-particulate SOM, listed from the lowest to the highest as: low C soil < high C soil +
458 fine sand 50:50 mixture < high C soil original < high C soil with sand excluded. The gradient of
459 C levels in these materials was remarkably well related to Os concentration (Fig. 7). Occurrence
460 of such a relationship is a promising sign for future development of a tool for visualizing locations
461 of non-particulate SOM. Such tool is especially important given the major role that non-particulate
462 SOM plays in soil C accrual. Currently, a complete absence of any other means for *in situ* SOM
463 visualization at comparable scales warrants further exploration of this technique. A potential future
464 strategy for quantifying soil C spatial patterns based on the Os approach can consist of building a
465 soil C vs. Os calibration curve for the specific soil of interest. Then, the calibration curve can be

used to convert a 3D image of Os saturation into a 3D map of C spatial patterns within the soil matrix of the intact samples. Since SOM composition can vary substantially among different soils as well as within the profile of the same soil [16], such calibration curves will probably need to be developed specifically for each studied soil.

Figure 7. Os levels, S_{Os}, as calculated from Eq. (1), plotted versus soil organic C for the four studied soil materials. Shown are the means for the low C soil (data from Experiment 3) and high C soil (with sand excluded) (data from Experiment 1) and respective standard errors. Values from the two studied spheres with bulk high C soil and high C soil mixed with fine sand are shown as individual dots (data from Experiment 2). Black line is linear regression fitted to the data.

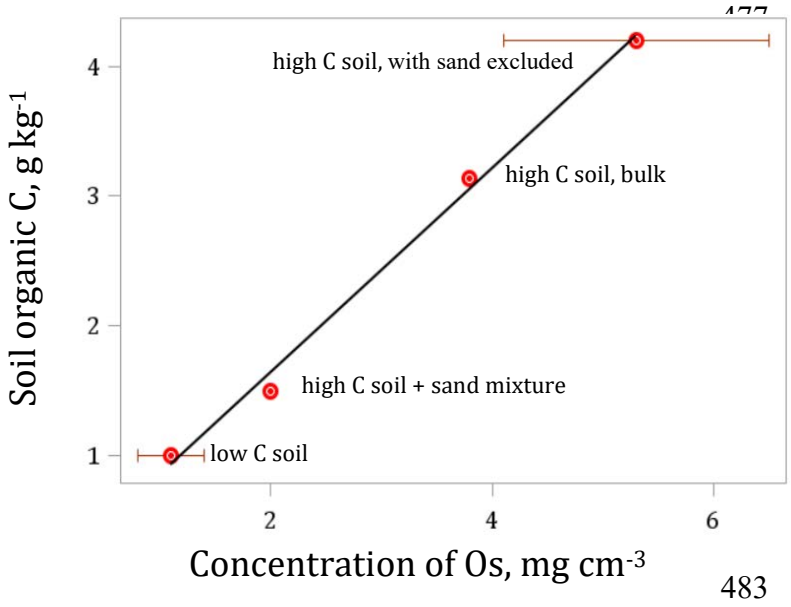

Our findings regarding the influence of pore-size distributions on the effectiveness of Os staining are controversial. On one hand, Os concentrations were not affected by the distance from the surface, i.e., by the length of the diffusion path for OsO_4 vapors, in either coarse or fine sands; and the differences between the two sands for the biochar and the high C soil inclusions were

relatively minor (Fig. 4). Also, there were only minor decreases in Os concentrations with the distance from the surface within the 50:50 sand plus soil mixture and within the high C soil-only sphere; the decrease that appeared only at 3-4 mm distances from the surface (Fig. 5). These observations suggest that the impediments to diffusion of OsO_4 vapors in the studied experimental conditions were relatively low. Os staining of the in-grown roots in Experiment 3 also supported negligible limitations of OsO_4 diffusion. Os concentrations in the small pore soil material and in the roots there were not significantly different from their large pore soil counterparts (Fig. 6).

But, on the other hand, the Os concentrations within the plant root inclusions in the coarse sand of Experiment 1 were substantially higher than those in the fine sand (Fig. 4). One possible explanation is that the two different roots that were used to prepare the root inclusion fragments for coarse and fine sand samples of our experiment differed in their content of C compounds with double C bonds. Further assessment of variability in Os staining efficiency of plant materials would be needed to determine plausibility of this explanation. However, even assuming that our root inclusion results are an artifact, we would recommend exercising caution when interpreting SOM estimations obtained via Os staining by passive diffusion of OsO_4 vapors at distances greater than 3-4 mm from the surface of the material or from the large pores within such material. Caution would be particularly warranted for the materials dominated by only few-micron sized pores.

Active explorations of OsO_4 applications in electron microscopy started >75 years ago [51] and since then OsO_4 has been widely used for visualization of unsaturated lipids and membranous structures [52]. Thus, even though OsO_4 is highly toxic, the protocols for its safe use for staining samples have long been tested and in-place. In our experience, the approach for staining soil samples with OsO_4 vapors did not differ from that needed for cell and tissue samples, and, overall, was much less time and cost consuming than many standard soil measurements. Getting access to

a synchrotron source for dual-energy scanning of the stained samples is probably the only main challenge that might face the researchers interested in implementing the method. Yet, globally, the synchrotron sources are offering free access and assistance to public research projects and dual-energy capabilities for Os determination are available at several such facilities.

ASSOCIATED CONTENT

Supporting Information:

Data generated during experimental phase of the current study (Excel)

Supplemental Table 1. Calculations of the percent of total C within the studied materials that responded to OsO_4 staining (PDF)

ACKNOWLEDGEMENT

We thank Maxwell Oerther for help with laboratory analysis, Abby Vanderberg for help with Os staining, and Yulia Shapovalova for organic chemistry advices.

Support for this research was provided in part by the NSF DEB Program (Award # 1904267), by the NSF LTER Program (DEB 1027253) at the Kellogg Biological Station, by USDA NC1187 project, by the Great Lakes Bioenergy Research Center, U.S. Department of Energy, Office of Science, Office of Biological and Environmental Research under Award Number DE-SC0018409, and by Michigan State University AgBioResearch. This research used resources of the Advanced Photon Source, a U.S. Department of Energy (DOE) Office of Science User Facility operated for the DOE Office of Science by Argonne National Laboratory under Contract No. DE-AC02-06CH11357. We acknowledge the support of GeoSoilEnviroCARS (Sector 13), which is

534 supported by the National Science Foundation - Earth Sciences (EAR-1128799), and the
535 Department of Energy, Geosciences (DE-FG02-94ER14466).

536

537 **REFERENCES**

538 1. Janzen, H., Carbon cycling in earth systems—a soil science perspective. *Agriculture,*
539 *Ecosystems & Environment* **2004,** *104*, (3), 399-417.
540 2. Lal, R., Soil erosion and the global carbon budget. *Environment International* **2003,** *29*,
541 (4), 437-450.
542 3. Lal, R.; Kimble, J. In *Conservation tillage for carbon sequestration.*, Int. Symp. on Soil-
543 Source and Sink of Greenhouse Gases. 18–21 Sept. 1995, Nanjing, China, 1997; Kluwer:
544 Nanjing, China, 1997; pp 243-253.
545 4. Reeves, D., The role of soil organic matter in maintaining soil quality in continuous
546 cropping systems. *Soil and Tillage Research* **1997,** *43*, (1-2), 131-167.
547 5. Singh, K. K.; Colvin, T.; Erbach, D.; Mughal, A., Tilth index: an approach to quantifying
548 soil tilth. *T Asae* **1992,** *35*, (6), 1777-1785.
549 6. Bauer, A.; Black, A., Quantification of the effect of soil organic matter content on soil
550 productivity. *Soil Sci Soc Am J* **1994,** *58*, (1), 185-193.
551 7. Radke, J.; Berry, E., Infiltration as a tool for detecting soil changes due to cropping,
552 tillage, and grazing livestock. *American Journal of Alternative Agriculture* **1993,** *8*, (4), 164-174.
553 8. Dungait, J. A.; Hopkins, D. W.; Gregory, A. S.; Whitmore, A. P., Soil organic matter
554 turnover is governed by accessibility not recalcitrance. *Global Change Biol* **2012,** *18*, (6), 1781-
555 1796.
556 9. Schmidt, M. W.; Torn, M. S.; Abiven, S.; Dittmar, T.; Guggenberger, G.; Janssens, I. A.;
557 Kleber, M.; Kögel-Knabner, I.; Lehmann, J.; Manning, D. A., Persistence of soil organic matter
558 as an ecosystem property. *Nature* **2011,** *478*, (7367), 49.
559 10. Six, J.; Elliott, E.; Paustian, K., Soil macroaggregate turnover and microaggregate
560 formation: a mechanism for C sequestration under no-tillage agriculture. *Soil Biology and*
561 *Biochemistry* **2000,** *32*, (14), 2099-2103.
562 11. Rabot, E.; Wiesmeier, M.; Schlüter, S.; Vogel, H.-J., Soil structure as an indicator of soil
563 functions: a review. *Geoderma* **2018,** *314*, 122-137.
564 12. Kravchenko, A. N.; Negassa, W. C.; Guber, A. K.; Rivers, M. L., Protection of soil
565 carbon within macro-aggregates depends on intra-aggregate pore characteristics. *Scientific*
566 *Reports* **2015,** *5*.
567 13. Mooney, S. J.; Pridmore, T. P.; Helliwell, J.; Bennett, M. J., Developing X-ray Computed
568 Tomography to non-invasively image 3-D root systems architecture in soil. *Plant Soil* **2012,** *352*,
569 (1-2), 1-22.
570 14. Piccoli, I.; Dal Ferro, N.; Delmas, P. J.; Squartini, A.; Morari, F., Contrast-enhanced
571 repacked soil cores as a proxy for soil organic matter spatial arrangement. *Soil Res* **2019,** *57*, (6),
572 535-545.
573 15. Van Loo, D.; Bouckaert, L.; Leroux, O.; Pauwels, E.; Dierick, M.; Van Hoorebeke, L.;
574 Cnudde, V.; De Neve, S.; Sleutel, S., Contrast agents for soil investigation with X-ray computed
575 tomography. *Geoderma* **2014,** *213*, 485-491.

16. Lehmann, J.; Solomon, D.; Kinyangi, J.; Dathe, L.; Wirick, S.; Jacobsen, C., Spatial complexity of soil organic matter forms at nanometre scales. *Nature Geoscience* **2008,** *1*, (4), 238.
17. Mueller, C. W.; Weber, P. K.; Kilburn, M. R.; Hoeschen, C.; Kleber, M.; Pett-Ridge, J., Advances in the analysis of biogeochemical interfaces: NanoSIMS to investigate soil microenvironments. In *Advances in Agronomy*, Elsevier: 2013; Vol. 121, pp 1-46.
18. Peth, S.; Chenu, C.; Leblond, N.; Mordhorst, A.; Garnier, P.; Nunan, N.; Pot, V.; Ogurreck, M.; Beckmann, F., Localization of soil organic matter in soil aggregates using synchrotron-based X-ray microtomography. *Soil Biol Biochem* **2014,** *78*, 189-194.
19. Chenu, C.; Plante, A. F., Clay-sized organo-mineral complexes in a cultivation chronosequence: revisiting the concept of the 'primary organo-mineral complex'. *Eur J Soil Sci* **2006,** *57*, (4), 596-607.
20. Rawlins, B. J. W., J.; Reinhard C.; Atwood R.C.; Houston, A.; Lark, R.M.; Rudolph, S., Three-dimensional soil organic matter distribution, accessibility and microbial respiration in macroaggregates using osmium staining and synchrotron X-ray computed tomography. *SOIL* **2016,** *2*, 659–671.
21. Quigley, M. Y.; Rivers, M. L.; Kravchenko, A. N., Patterns and Sources of Spatial Heterogeneity in Soil Matrix From Contrasting Long Term Management Practices. *Frontiers in Environmental Science* **2018,** *6*.
22. Griffiths, W., Osmium tetraoxide and its applications. *Platinum Metals Review* **1974,** *18*, (3), 94-96.
23. Belazi, D.; Sole-Domenech, S.; Johansson, B.; Schalling, M.; Sjovall, P., Chemical analysis of osmium tetroxide staining in adipose tissue using imaging ToF-SIMS. *Histochem Cell Biol* **2009,** *132*, (1), 105-115.
24. Bahr, G. F., Osmium Tetroxide and Ruthenium Tetroxide and Their Reactions with Biologically Important Substances - Electron Stains Iii. *Exp Cell Res* **1954,** *7*, (2), 457-479.
25. Derenne, S.; Quenea, K., Analytical pyrolysis as a tool to probe soil organic matter. *J Anal Appl Pyrol* **2015,** *111*, 108-120.
26. Robertson, G. P.; Hamilton, S. K., Long-term ecological research in agricultural landscapes at the Kellogg Biological Station LTER site: conceptual and experimental framework. In *The ecology of agricultural landscapes: long-term research on the path to sustainability*, Hamilton, S. K.; Doll, J. E.; Robertson, G. P., Eds. Oxford University Press: New York, New York, USA., 2015; pp 1-32.
27. Toosi, E. R.; Kravchenko, A. N.; Guber, A. K.; Rivers, M. L., Pore characteristics regulate priming and fate of carbon from plant residue. *Soil Biol Biochem* **2017,** *113*, 219-230.
28. Hayes, T. L.; Lindgren, L. T.; Gofman, J. W., A quantitative determination of the osmium tetroxide-lipoprotein interaction. *J Cell Biol* **1963,** *19*, 251-255.
29. Rasband, W. S. ImageJ. http://rsb.info.nih.gov/ij/ (May 15),
30. Schindelin, J.; Arganda-Carreras, I.; Frise, E.; Kaynig, V.; Longair, M.; Pietzsch, T.; Preibisch, S.; Rueden, C.; Saalfeld, S.; Schmid, B.; Tinevez, J. Y.; White, D. J.; Hartenstein, V.; Eliceiri, K.; Tomancak, P.; Cardona, A., Fiji: an open-source platform for biological-image analysis. *Nat Methods* **2012,** *9*, (7), 676-682.
31. Hubbell, J. H.; Seltzer, S. M., X-Ray Mass Attenuation Coefficients. In NIST Standard Reference Database 126., 1996.

32. Munch, B.; Holzer, L., Contradicting Geometrical Concepts in Pore Size Analysis Attained with Electron Microscopy and Mercury Intrusion. *J Am Ceram Soc* **2008,** *91*, (12), 4059-4067.
33. Munch, E. A., User's Guide to Topological Data Analysis. *Journal of Learning Analytics* **2017,** *4*, (2), 47-61.
34. Kittler, J.; Illingworth, J., Minimum Error Thresholding. *Pattern Recogn* **1986,** *19*, (1), 41-47.
35. Baker, J., Fixation in cytochemistry and electron microscopy. In *9th annual meeting of the Histochemical Society*, Philadelphia, 1958.
36. Nielson, A. J.; Griffith, W. P., Tissue Fixation by Osmium-Tetroxide - Possible Role for Proteins. *J Histochem Cytochem* **1979,** *27*, (5), 997-999.
37. Korn, E. D., A Chromatographic and Spectrophotometric Study of Products of Reaction of Osmium Tetroxide with Unsaturated Lipids. *J Cell Biol* **1967,** *34*, (2), 627-&.
38. Kravchenko, A. N.; Negassa, W.; Guber, A. K.; Schmidt, S., New Approach to Measure Soil Particulate Organic Matter in Intact Samples using X-Ray Computed Microtomography. *Soil Sci Soc Am J* **2014,** *78*, (4), 1177-1185.
39. Arachchige, P. S. P.; Hettiarachchi, G. M.; Rice, C. W.; Dynes, J. J.; Maurmann, L.; Wang, J.; Karunakaran, C.; Kilcoyne, A. L. D.; Attanayake, C. P.; Amado, T. J. C.; Fiorin, J. E., Sub-micron level investigation reveals the inaccessibility of stabilized carbon in soil microaggregates. *Scientific Reports* **2018,** *8*.
40. Kinyangi, J.; Solomon, D.; Liang, B. I.; Lerotic, M.; Wirick, S.; Lehmann, J., Nanoscale biogeocomplexity of the organomineral assemblage in soil: Application of STXM microscopy and C 1s-NEXAFS spectroscopy. *Soil Sci Soc Am J* **2006,** *70*, (5), 1708-1718.
41. Koestel, J.; Larsbo, M.; Jarvis, N., Scale and REV analyses for porosity and pore connectivity measures in undisturbed soil. *Geoderma* **2020,** *366*.
42. Borges, J. A. R.; Pires, L. F.; Cassaro, F. A. M.; Roque, W. L.; Heck, R. J.; Rosa, J. A.; Wolf, F. G., X-ray microtomography analysis of representative elementary volume (REV) of soil morphological and geometrical properties. *Soil and Tillage Research* **2018,** *182*, 112-122.
43. MacCarthy, P., The principles of humic substances. *Soil Sci* **2001,** *166*, (11), 738-751.
44. Kelleher, B. P.; Simpson, A. J., Humic substances in soils: Are they really chemically distinct? *Environmental Science & Technology* **2006,** *40*, (15), 4605-4611.
45. Schumacher, M.; Christl, I.; Scheinost, A. C.; Jacobsen, C.; Kretzschmar, R., Chemical heterogeneity of organic soil colloids investigated by scanning transmission X-ray microscopy and C-1s NEXAFS microspectroscopy. *Environmental Science & Technology* **2005,** *39*, (23), 9094-9100.
46. Onstad, G. D.; Canfield, D. E.; Quay, P. D.; Hedges, J. I., Sources of particulate organic matter in rivers from the continental USA: Lignin phenol and stable carbon isotope compositions. *Geochim Cosmochim Ac* **2000,** *64*, (20), 3539-3546.
47. Solomon, D.; Lehmann, J.; Harden, J.; Wang, J.; Kinyangi, J.; Heymann, K.; Karunakaran, C.; Lu, Y.; Wirick, S.; Jacobsen, C., Micro-and nano-environments of carbon sequestration: Multi-element STXM–NEXAFS spectromicroscopy assessment of microbial carbon and mineral associations. *Chem Geol* **2012,** *329*, 53-73.
48. Singh, B.; Fang, Y.; Cowie, B. C.; Thomsen, L., NEXAFS and XPS characterisation of carbon functional groups of fresh and aged biochars. *Org Geochem* **2014,** *77*, 1-10.

664 49. Sousa, A. A.; Hohmann-Marriott, M.; Aronova, M. A.; Zhang, G.; Leapman, R. D.,
665 Determination of quantitative distributions of heavy-metal stain in biological specimens by
666 annular dark-field stem. *Journal of Structural Biology* **2008,** *162*, 14-28.
667 50. Collard, F. X.; Blin, J., A review on pyrolysis of biomass constituents: Mechanisms and
668 composition of the products obtained from the conversion of cellulose, hemicelluloses and
669 lignin. *Renew Sust Energ Rev* **2014,** *38*, 594-608.
670 51. Porter, K. R.; Claude, A.; Fullam, E. F., A study of tissue culture cells by electron
671 microscopy. *Journal of Experimental Medicine* **1945,** *81*, 233-246

672
673 52. Bozzola, J. J.; Russell, L. D., Specimen preparation for transmission electron microscopy.
674 In *Electron Microscopy: Principles and Techniques for Biologists*, Jones and Bartlett publishers:
675 Sudbury, Massachusetts, 1999; pp 21-31.

676

677

Supporting information

Title:

Testing Os staining approach for visualizing soil organic matter patterns in intact samples via X-ray dual-energy tomography scanning

Authors:

Hongbing Zheng[12], Kyungmin Kim[1], Alexandra Kravchenko[1]*, Mark Rivers[3], Andrey Guber[1]

Affiliations:

[1] Department of Plant, Soil and Microbial Sciences, Michigan State University, East Lansing, MI, United States

[2] Research Institute of Agricultural Resources and Environment, Jilin Academy of Agricultural Science, Changchun, 130033, China

[3] Argonne National Lab, Center for Advanced Radiation Sources, the University of Chicago, Chicago, IL, United States

***Corresponding Author:**

Department of Plant, Soil and Microbial Sciences, Michigan State University, East Lansing, MI, 48824, United States.

E-mail: kravche1@msu.edu

Supplemental Table 1. Calculations of the percent of total C within the studied materials that responded to OsO_4 staining.

Material	Os, mg cm^{-3}	Total C in the Material, %	Bulk density of the Material, g/cm^3	C in cm^3 of the Material, g	C in cm^3 of the Material, N C atoms	Average amount of Os in cm^3 of the Material, g	Average amount of Os in cm^3 of the Material, N atoms	Max amount of C (4 C atoms per one Os) reacted with one cm^3 of the Material, N atoms	Max amount of C reacted with one cm^3 of the Material, g	% of C that responded to Os
Switchgrass roots	8.4	39.4	0.80	0.312	1.57E+22	8.41E-03	2.66E+19	1.06E+20	2.12E-03	0.7
High C soil, sand free	5.3	4.2	1.00	0.0417	2.09E+21	5.30E-03	1.68E+19	6.71E+19	1.34E-03	3.2
High C soil, bulk	3.7	3.0	1.10	0.0330	1.66E+21	3.75E-03	1.19E+19	4.74E+19	9.45E-04	2.9
High C soil + fine sand (50:50)	2.0	1.5	1.12	0.0168	8.43E+20	1.99E-03	6.31E+18	2.52E+19	5.03E-04	3.0
Low C soil	1.1	1.0	1.25	0.0125	6.27E+20	1.08E-03	3.41E+18	1.36E+19	2.71E-04	2.2
Biochar	1.8	64.9	0.40	0.260	1.30E+22	1.83E-03	5.80E+18	2.32E+19	4.62E-04	0.2
Fine sand	-0.1	0	1.14	0						NA
Coarse sand	-0.2	0	1.18	0						NA